Population Trends of Spanwise Vortices in Wall Turbulence

By Y. WU[1] AND K. T. CHRISTENSEN[1,2]†

[1]Department of Theoretical and Applied Mechanics, University of Illinois
Urbana, IL 61801, USA

[2]Department of Mechanical and Industrial Engineering, University of Illinois
Urbana, IL 61801, USA

The present effort documents the population trends of prograde and retrograde spanwise vortex cores in wall turbulence outside the buffer layer. Large ensembles of instantaneous velocity fields are acquired by particle-image velocimetry in the streamwise–wall-normal plane of both turbulent channel flow at $\mathrm{Re}_\tau \equiv u_*\delta/\nu = 570$, 1185 and 1760 and a zero-pressure-gradient turbulent boundary layer at $\mathrm{Re}_\tau = 1400$, 2350 and 3450. Substantial numbers of prograde spanwise vortices are found to populate the inner boundary of the log layer of both flows and most of these vortices have structural signatures consistent with the heads of hairpin vortices. In contrast, retrograde vortices are most prominent at the outer edge of the log layer, often nesting near clusters of prograde vortices. Resolved prograde population densities display $\mathrm{Re}_\tau^{3/2}$ dependence in the region $100 < y^+ < 0.5\delta^+$ while their retrograde counterparts display a similar dependence for $y < 0.35\delta$, except for the $\mathrm{Re}_\tau = 570$ case. In addition, similarity in the fractions of resolved prograde and retrograde spanwise vortices is observed for $100 < y^+ < 0.8\delta^+$ in channel flow and in both flows for $100 < y^+ < 0.3\delta^+$ over the Re_τ range studied. The fraction of retrograde vortices increases slightly with Re_τ beyond the log layer in both flows, suggesting that they may play an increasingly-important role at higher Reynolds numbers. Finally, while the overall prograde and retrograde population trends of channel flow and the boundary layer show little difference for $y < 0.45\delta$, the retrograde populations differ considerably beyond this point, highlighting the influence of the opposing wall in channel flow.

1. Introduction

The results of many recent experimental and computational studies suggest that wall turbulence is populated by hairpin vortices that tend to streamwise-align into larger-scale coherent groups termed vortex packets (The phrase "hairpin vortex" is used to describe both symmetric and asymmetric hairpin-, lambda- and arch-like structures.). These hairpin structures are comprised of either one or two streamwise-oriented legs connected to a spanwise-oriented head whose rotation is of the same sense as the mean shear (hereafter referred to as a 'prograde' spanwise vortex) and are qualitatively consistent with the horseshoe vortex first proposed by Theodorsen (1952). At low Reynolds number (Re), Smith (1984) reported the existence of hairpin vortices and suggested an organized alignment of these structures in the streamwise direction. Smith *et al.* (1991) later showed that hairpin vortices can regenerate from an existing vortex. Similar organization and regeneration was noted by Zhou *et al.* (1999) who studied the evolution of an initial hairpin-like structure in the mean turbulent field of a low-Re channel flow via direct

† Author to whom correspondence should be addressed: ktc@uiuc.edu

numerical simulation (DNS). Given sufficient strength of the initial structure, multiple hairpin vortices spawned both upstream and downstream of the initial structure, creating a coherent train of vortices. The legs of vortices residing in the log layer were commonly observed to extend below $y^+ \equiv y/y_* = 60$ (y_* is the viscous length scale), consistent with the near-wall quasi-streamwise vortex observations of Brooke & Hanratty (1993) and Schoppa & Hussain (1997), among others. This work also illustrated a preference for asymmetric hairpins, with one leg often stronger than the other. The stereoscopic visualizations of Delo *et al.* (2004) complement these efforts by providing three-dimensional views of this organization at low-Re. Their results highlight the contorted nature of the small-scale vortices that agglomerate to form larger-scale structures and further support the coupling between near-wall ejections and the passage of large-scale motions.

At higher Re, Head & Bandyopadhyay (1981) observed ramp-like patterns at the outermost edge of a turbulent boundary layer and proposed these patterns to be the imprint of groups of hairpin vortices inclined away from the wall. More recently, particle-image velocimetry (PIV) measurements at moderate Re in a turbulent boundary layer by Adrian *et al.* (2000*b*) provide evidence that hairpin structures occur throughout the outer layer and streamwise-align to create larger-scale vortex packets. The PIV data permitted visualization of this organization in the streamwise–wall-normal plane within the interior of the boundary layer, showing that packets occur throughout the outer region in a hierarchy of scales. This scale hierarchy is consistent with the mechanisms proposed by Perry & Chong (1982) and Tomkins & Adrian (2003) provide direct evidence of spanwise scale growth via merging on an eddy-by-eddy basis up to $y^+ = 100$ and present scenarios by which this scale growth might manifest itself for $y^+ > 100$. Finally, the efforts of Liu *et al.* (2001) and Ganapathisubramani *et al.* (2003) underscore the important role these large-scale motions play in log-layer transport processes.

While prograde spanwise vortices in the form of hairpin heads are often observed in the outer layer of wall turbulence, vortical motions with positive ω_z signatures, 'retrograde' spanwise vortices, are also known to exist. The flow-visualization studies of Falco (1977) in the streamwise–wall-normal plane of a turbulent boundary layer revealed counter-rotating vortex pairs at the outer edge of the boundary layer (spatially-coincident retrograde and prograde spanwise vortex cores). These "typical eddies" exhibited spatial characteristics consistent with localized ring-like structures (Klewicki *et al.* 1990). Subsequent efforts by Falco and co-workers determined that such structures often originate in the outer layer and advect into the near-wall region, initiating inner-/outer-layer interactions that can actively lead to the generation of near-wall structure, including hairpin structures (Falco 1977, 1983, 1991). This inner-/outer-layer interaction model is further supported by the recent efforts of Klewicki & Hirschi (2004) who consistently observed hairpin vortices and retrograde structures clustered in the neighborhood of intense near-wall shear layers, with the influence of retrograde structures increasing with Reynolds number. Further, the aforementioned stereoscopic visualizations of Delo *et al.* (2004) revealed the presence of loops and mushroom-like patterns which, if sliced in the streamwise–wall-normal plane, would exhibit retrograde and prograde signatures.

While the origin of retrograde spanwise vortices is not yet understood, several possibilities have been reported that link their formation to hairpin structures. Yang *et al.* (2001) used a passive mixing tab to generate trains of hairpin vortices in a laminar boundary layer and observed the formation of retrograde spanwise vortices just below and upstream of strong hairpin structures. Alternatively, the efforts of Moin *et al.* (1986), Melander & Zabuski (1988) and Smith *et al.* (1991) revealed that the legs of hairpin structures can, under certain conditions, pinch off and reconnect to form localized ring-like structures. Further, Tomkins & Adrian (2003) proposed the generation of isolated retrograde span-

wise vortices via the spanwise interaction of hairpin structures. Finally, it is also possible that spatially-coincident prograde and retrograde spanwise vortices may in fact belong to a single hairpin structure. Klewicki (1997) found that hairpin vortices can turn in the spanwise direction, yielding pairs of counter-rotating spanwise vortices associated with the legs of the hairpin. Another possibility is a hairpin structure with an omega shape around its shoulders and head. If such a structure were sliced in the streamwise–wall-normal plane through one of its shoulders, a pair of prograde and retrograde structures may be revealed with the prograde core oriented above and downstream of the retrograde core since hairpins are normally inclined at roughly 45° from the wall. This orientation is consistent with the patterns observed by Yang *et al.* (2001) in their mixing-tab experiments, although they do not address such a possibility.

The intent of the present effort is to document the population trends of prograde and retrograde spanwise vortices as a function of wall-normal position, Reynolds number and flow. Such information is often required in structure-based models of wall turbulence, like the attached-eddy model of Perry & Marusic (1995) which was recently extended by Marusic (2001) to include the possibility of coherent vortex organization. Particle-image velocimetry (PIV) measurements are made in the streamwise–wall-normal plane of turbulent channel flow and a zero-pressure-gradient turbulent boundary layer. A vortex identification method is used to extract the resolved vortices from the background turbulence, facilitating detailed population studies of these structures.

2. Experiments

2.1. *Flow facilities*

The channel-flow facility utilized in this effort has a development length of 252δ (where $\delta = 25\,\mathrm{mm}$ is the half-height of the channel) and an aspect ratio of 12:1. The working fluid of the facility is air and the flow is conditioned by a series of screens, a honeycomb and a contraction. The flow is then tripped upon entrance to the channel with 36-grit sandpaper, ensuring fully-developed flow at the test section. Glass windows in the test section provide optical access from all directions while static pressure taps mounted along the length of the channel development facilitate independent evaluation of the wall shear stress (τ_w). Fluid properties are assessed from measurements of the atmospheric pressure and fluid temperature using an ideal gas relation in concert with Sutherland's correlation for viscosity. These flow and fluid properties are then used to determine the friction velocity, $u_* \equiv (\tau_w/\rho)^{1/2}$, and the viscous length scale, $y_* \equiv \nu/u_*$, at each Re.

The turbulent-boundary-layer measurements are made under zero-pressure-gradient conditions in a low-turbulence, open-circuit boundary-layer wind tunnel. This facility has a documented turbulence intensity of 0.16% in the free-stream and the boundary layer develops over a 6.1 m-long hydraulically-smooth flat plate that has an elliptically-shaped leading edge and is mounted 100 mm above the bottom surface of the 457 mm-tall test section (Meinhart 1994). The flow is tripped far upstream of the measurement location and optical access to the boundary layer is provided from the side and below by float glass windows. Fluid properties are determined in the same manner as with the channel-flow experiments; however, u_* and y_* are assessed using the Clauser chart method. Table 1 summarizes the relevant flow parameters for all flow conditions studied.

2.2. *Velocity measurements*

Particle-image velocimetry is used to measure instantaneous, two-dimensional velocity (u, v) fields in the streamwise–wall-normal $(x - y)$ plane of turbulent channel and boundary-layer flows. The channel-flow measurements are made at $\mathrm{Re}_\tau \equiv u_*\delta/\nu = 570$,

	Re_τ	δ	U_∞	u_*	y_*	Δx^+	Δy^+	Δz^+	No. of	Symbol
	–	(mm)	(m/s)	(m/s)	(μm)	–	–	–	Realizations	–
Channel	570	25.0	8.6	0.41	44.1	9.3	9.3	4.5	2000	□
	1185	25.0	19.0	0.86	21.1	9.7	9.7	9.5	2000	○
	1760	25.0	29.7	1.27	14.2	9.0	9.0	14.1	2000	▽
TBL	1400	87.4	6.5	0.25	62.4	10.9	10.9	8.0	2500	■
	2350	103.1	9.9	0.36	43.9	12.3	12.3	11.4	2500	●
	3450	96.0	16.1	0.56	27.8	11.2	11.2	18.0	2499	▼

TABLE 1. Summary of flow parameters for all experiments.

1185 and 1760 with a field of view of $1.3\delta \times \delta$ (streamwise × wall-normal) confined between the bottom wall and the centerline of the channel. The boundary-layer measurements are made at $\mathrm{Re}_\tau = 1400$, 2350 and 3450 (equivalently $\mathrm{Re}_\theta \equiv U_\infty \theta/\nu = 3870$, 8330 and 10730, where θ is the momentum thickness and U_∞ is the free-stream velocity) with a field of view of $\delta \times \delta$ at the two lower Re and $1.45\delta \times \delta$ at the highest Re. The flows are seeded with 1 μm olive-oil droplets and the fields of view are illuminated with lightsheets formed from a pair of Nd:YAG lasers. The lightsheets have a spanwise thickness of $\Delta z \simeq 200\,\mu$m and 500 μm in the channel and boundary-layer cases, respectively. A $1.3\mathrm{k} \times 1\mathrm{k}$ pixel 12-bit CCD camera is used to image the particles in the channel-flow cases while the boundary-layer measurements are achieved with a $2\mathrm{k} \times 2\mathrm{k}$ pixel 12-bit CCD camera at $\mathrm{Re}_\tau = 1400$ and 2350 and a $4\mathrm{k} \times 2.8\mathrm{k}$ pixel 12-bit CCD camera at $\mathrm{Re}_\tau = 3450$. Time delays are selected to ensure a relative velocity measurement error of less than 1% in all cases.

The pairs of PIV images are subdivided into square interrogation windows and a larger second window is selected to minimize bias errors associated with loss of image pairs. The images are analyzed using two-frame cross-correlation methods with 50% overlap to satisfy Nyquist's criterion and the second window is offset in the mean flow direction by the bulk displacement of the flow. Since our interest lies in studying the properties of smaller-scale spanwise vortices whose diameters appear to scale with y_* (Carlier & Stasnislas 2005), the size of the first interrogation window is chosen such that the vector grid spacing at each Re_τ is consistent in inner units. To meet this requirement, the dimensions of the first interrogation windows are chosen to yield vector grid spacings, Δx and Δy, of approximately $9.0y_*$ for all three channel-flow Re_τ and $11y_*$ for the three boundary-layer Re_τ (see table 1). The instantaneous vector fields are then validated using standard deviation and local magnitude difference comparisons to remove erroneous velocity vectors. The few holes created by this validation process are filled either with alternative velocity choices determined during the interrogation or interpolated in regions where at least 50% of neighbors are present. Each vector field is then low-pass filtered with a narrow Gaussian filter to remove any noise associated with frequencies larger than the sampling frequency of the interrogation.

3. Vortex identification

Accurate assessment of the population trends of prograde and retrograde spanwise vortices requires the identification and extraction of such structures from the background turbulence. Galilean decomposition via removal of a fixed advection velocity from an instantaneous velocity field represents one method for uncovering vortices advecting at similar speeds and is often the best choice when one wishes to study the local motions induced by these structures. In particular, when the chosen advection velocity matches

the streamwise velocity of a vortex it becomes recognizable as a roughly circular pattern of vectors representing closed streamlines, consistent with the definition of a vortex offered by Kline & Robinson (1989). Unfortunately, since the advection velocity of a given vortex in a wall-bounded flow can depend upon its position relative to the wall, one must remove a broad range of advection velocities in order to reveal all embedded structure.

Alternatively, vortical structures can be identified through analysis of the local velocity gradient tensor (Chong *et al.* 1990; Zhou *et al.* 1999, for example). Swirling strength utilizes the imaginary part of the complex eigenvalue of the local velocity gradient tensor (λ_{ci}) to reveal embedded structure (Zhou *et al.* 1999). The local velocity gradient tensor has one real eigenvalue (λ_r) and a pair of complex-conjugate eigenvalues ($\lambda_{cr} \pm i\lambda_{ci}$) in three dimensions when the discriminant of its characteristic equation is positive. In this context, λ_{ci}^{-1} represents the period required for a fluid particle to swirl once about the λ_r-axis. Hence, $\lambda_{ci} \neq 0$ identifies the presence of local swirling, meaning that spatially-connected regions of non-zero λ_{ci} represent vortices. Vortex identification via swirling strength is Galilean invariant and does not identify regions of intense shear that are absent of rotation. However, since PIV fields are inherently 2-D, an equivalent form of $\nabla\mathbf{u}$ is computed in the plane in which the PIV data resides and clusters of non-zero λ_{ci} represent vortex sections in this plane (Adrian *et al.* 2000*a*). However, while swirling strength is found to accurately identify structure embedded in turbulent velocity fields, it still has one primary deficiency: it does not yield the sense of the identified rotation. Therefore, a swirling-strength parameter of the form

$$\Lambda_{ci}(x,y) \equiv \lambda_{ci}(x,y)\frac{\omega_z(x,y)}{|\omega_z(x,y)|}, \tag{3.1}$$

is introduced where ω_z is the instantaneous fluctuating spanwise vorticity. This modified swirling-strength is analogous to the one employed by Tomkins & Adrian (2003) in wall-parallel PIV planes and yields clear distinction between vortices with counterclockwise and clockwise rotation (the phrase "swirling strength" hereon refers to Λ_{ci}).

In order to illustrate the virtues of Λ_{ci} as a vortex identification tool, it is contrasted with Galilean decomposition using an instantaneous channel-flow velocity field in the streamwise–wall-normal plane at $\mathrm{Re}_\tau = 1185$. Galilean decomposition of this instantaneous field with an advection velocity of $0.8U_\infty$ (figure 1(a)) reveals only those spanwise vortices advecting at this speed. Several swirling patterns consistent with the Kline & Robinson (1989) definition of a vortex are noted near $y = 0.2\delta$. Contours of instantaneous Λ_{ci} are also shown in the background of figure 1(a) and clusters of Λ_{ci} are noted at all locations where swirling motions are present in the Galilean-decomposed velocity field. Clusters of Λ_{ci} are also observed at numerous spatial locations where vortices are not apparent in the Galilean decomposition because these structures are not travelling at the chosen advection velocity. One can confirm that all of these Λ_{ci} clusters represent embedded swirling motions by performing a local Galilean decomposition in the immediate vicinity of each Λ_{ci} cluster in figure 1(a). This local decomposition, shown in figure 1(b), confirms that all regions of non-zero Λ_{ci} are indeed associated with embedded closed streamline patterns in the spirit of the Kline & Robinson (1989) definition. Further, figure 1(b) highlights the large populations of both prograde and retrograde spanwise vortices that can exist in wall-bounded turbulence as 26 spanwise vortices (8 retrograde and 18 prograde) are identified in this particular realization. Finally, these vortex cores represent spanwise sections of vortices since their orientations relative to the measurement plane cannot be determined from the two-dimensional fields.

A crucial consideration in the identification of vortical structures via Λ_{ci} is the threshold one selects for identifying the boundaries of the vortex sections (The example pre-

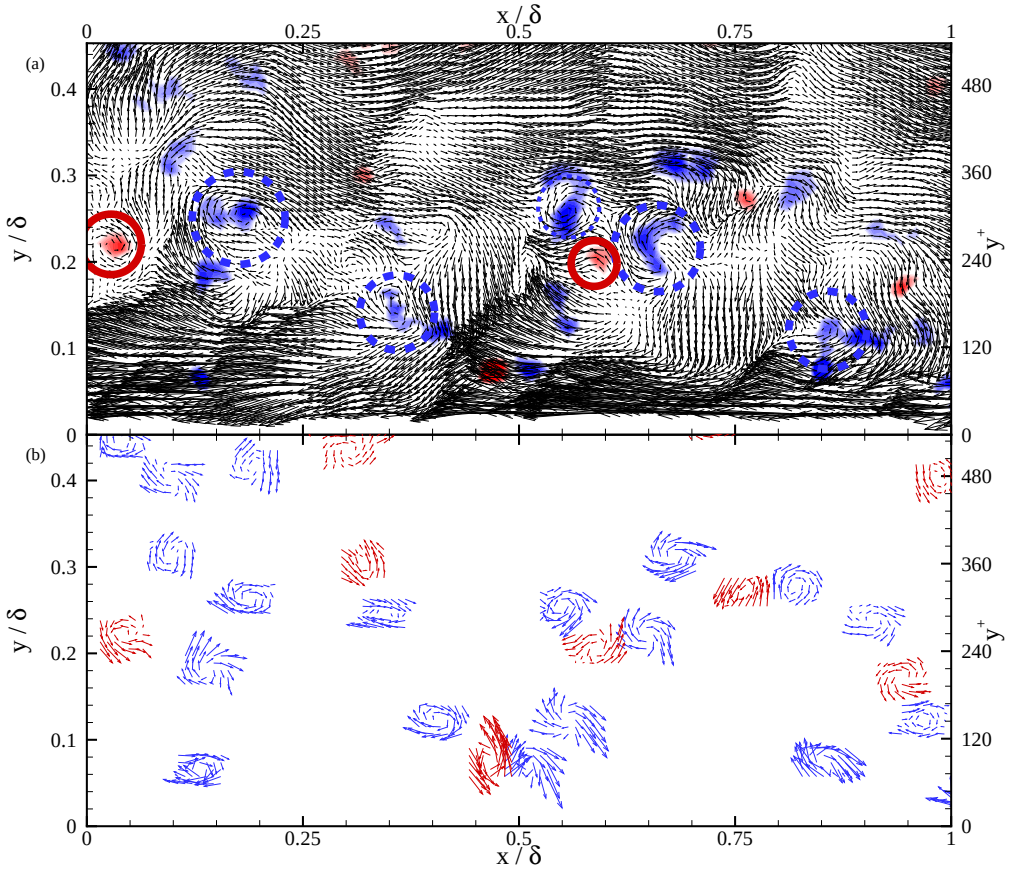

FIGURE 1. Example of vortex identification and extraction in an instantaneous, two-dimensional PIV velocity field acquired in turbulent channel flow at $\mathrm{Re}_\tau = 1185$. (a) Galilean decomposition of the instantaneous velocity field at $U_c = 0.8U_\infty$ with contours of instantaneous Λ_{ci} in the background; (b) localized Galilean decomposition of vortices identified using Λ_{ci}. Retrograde spanwise vortices are presented in red and prograde vortices are highlighted in blue.

sented in figure 1 utilizes a threshold of $|\Lambda_{ci}(x,y)| \geqslant 1.5\Lambda_{ci}^{\mathrm{rms}}(y)$). Nagaosa & Handler (2003) encountered similar issues in the identification of vortices in a DNS of free-surface turbulence using the second invariant of $\nabla\mathbf{u}$, Q. They found that normalizing Q with its root-mean-square (RMS) at a given wall-normal location yielded nearly-identical probability density functions (pdf's) of $\widetilde{Q} = Q/Q_{\mathrm{rms}}(y)$, insensitive to Re and y. After considering a range of thresholds, Nagaosa & Handler (2003) selected the threshold $|\widetilde{Q}| = 1$ which clearly identified vortical structures throughout their DNS realizations. Since Q and λ_{ci} yield nearly identical vortex-identification results (Chakraborty *et al.* 2005), the selection of a universal Λ_{ci} threshold should also be possible. Figure 2 presents pdf's of $\widetilde{\Lambda}_{ci} = \Lambda_{ci}/\Lambda_{ci}^{\mathrm{rms}}(y)$ at several wall-normal locations for the $\mathrm{Re}_\tau = 570$ channel-flow and $\mathrm{Re}_\tau = 2350$ boundary-layer cases. These pdf's of $\widetilde{\Lambda}_{ci}$ are similar to those reported by Nagaosa & Handler (2003) for $\widetilde{Q}$, particularly in terms of their relative insensitivity to y and Re for $|\widetilde{\Lambda}_{ci}| < 4$ (Although not shown, similar pdf's of $\widetilde{\Lambda}_{ci}$ are obtained for all of the other Re_τ presented herein). The threshold $|\widetilde{\Lambda}_{ci}| = 1$ was attempted in the present effort; however, it yielded vortex sections with very jagged edges, indicating that this threshold

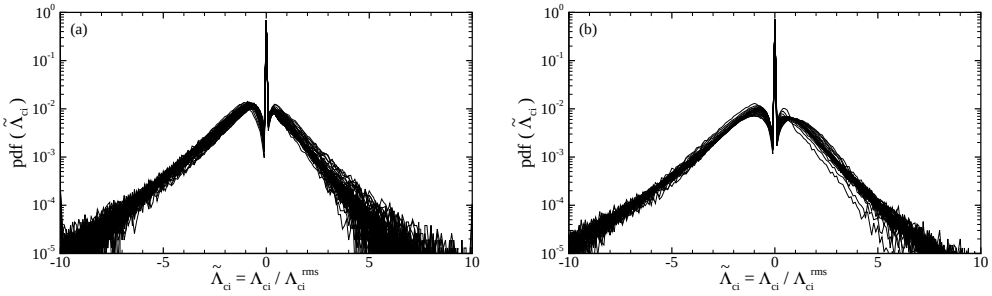

FIGURE 2. Probability density functions of $\widetilde{\Lambda}_{ci}$ for $100 < y^+ < 0.95\delta^+$ at (a) $\mathrm{Re}_\tau = 570$ (channel flow) and (b) $\mathrm{Re}_\tau = 2350$ (boundary layer).

level may be somewhat contaminated by the experimental noise associated with differentiation of the PIV data. While the inclusion of such edge noise does not alter the vortex populations appreciably, most notably their Reynolds-number and wall-normal trends and their scalings (the main contributions of this effort), it does change the space occupied by the cores which in turn alters the quantitative values of their mean shear contributions presented later. We therefore settled on a universal threshold $|\widetilde{\Lambda}_{ci}| = 1.5$, slightly larger than that used by Nagaosa & Handler (2003), which limits the influence of experimental noise associated with the calculation of $\nabla\mathbf{u}$ from the PIV measurements.

Further, the size of the smallest resolvable vortex section is inherently limited by the spatial resolution of the PIV measurements. As such, clusters of Λ_{ci} with fewer than three grid points across their span in both x and y satisfying $|\widetilde{\Lambda}_{ci}| \geqslant 1.5$ are not considered due to insufficient spatial resolution. Therefore, the spanwise vortices studied herein are necessarily limited to structures with cross-sectional lengths exceeding $18y_*$ and $22y_*$ in the channel-flow and boundary-layer datasets, respectively. The present analysis is also limited to the wall-normal region outside the buffer layer ($y^+ \gtrsim 100$) since the spatial resolution achieved is insufficient to fully resolve the flow beneath the log layer.

Finally, validation of this identification method is achieved by comparing the average cross-sectional length scales of the identified vortices with the recent results reported by Carlier & Stasnislas (2005) who used a Gaussian-vortex template as a vortex identifier. The area occupied by each vortex section in the $\mathrm{Re}_\tau = 2350$ ($\mathrm{Re}_\theta = 8830$) boundary-layer ensemble is assessed, yielding a measure of its cross-sectional length, $L = \sqrt{A}$ (This length scale was chosen instead of assuming a circular cross-section and computing a diameter since the orientation of the vortices relative to the measurement plane is not known). This Reynolds number was specifically chosen to directly compare against the $\mathrm{Re}_\theta = 8330$ log-layer diameter range $D = 40-50y_*$ ($L = 35-44y_*$ since $L = \frac{\sqrt{\pi}}{2}D$) reported in Carlier & Stasnislas (2005) (no distinction was made between prograde and retrograde structures). The present results yield an average length-scale range $L = 45 - 52y_*$ over a similar wall-normal region. While this range is slightly larger than that reported by Carlier & Stasnislas (2005), it should be noted that their PIV field of view was focused entirely within the log layer which allowed a finer spatial resolution to be achieved. As such, their average core diameters are influenced by structures smaller than can be resolved in the present effort. Nevertheless, the vortices identified via Λ_{ci} bear spatial characteristics consistent with results presented in the literature.

4. Examples of prograde and retrograde spanwise vortices

Before discussing the quantitative population trends of prograde and retrograde spanwise vortices, instantaneous examples of such structures are considered. Figure 3(a) presents an instantaneous velocity realization in the streamwise–wall-normal plane of turbulent channel flow at $\mathrm{Re}_\tau = 1185$ visualized via Galilean decomposition. Galilean decomposition is used in this section since it provides a view of the local kinematics in the reference frame of the visualized structures. Seven spanwise vortices are noted within the log layer in this instantaneous field: five are prograde vortices (denoted A–E) and two are retrograde structures (labelled F and G). The prograde structures appear to induce strong ejections of low-speed fluid just below and upstream of their cores, consistent with the hairpin vortex signature introduced by Adrian *et al.* (2000*b*). In addition, these prograde structures are aligned in the streamwise direction and are moving at nearly the same speed. As such, these hairpin vortices appear to form a vortex packet within the log layer and the collectively-induced ejections generate a large-scale region of relatively uniform low-momentum fluid beneath the streamwise-aligned vortices, consistent with the packet observations of Adrian *et al.* (2000*b*). Two retrograde structures, labelled F (spatially-coincident to prograde structure B) and G (spatially-coincident to prograde vortex E) are also noted in this Galilean decomposition. These retrograde spanwise vortices appear to nest along the "backbone" of the hairpin packet, similar to the scalar-visualization observations of Klewicki & Hirschi (2004).

Similar structural features are noted in an instantaneous velocity realization from the $\mathrm{Re}_\tau = 2350$ boundary-layer ensemble visualized by Galilean decomposition (figure 3(b)). Five spanwise vortices are revealed in this reference frame: four are prograde structures (labelled A–D) and the other is a retrograde structure (labelled E). The spatial characteristics of the prograde structures are consistent with the hairpin vortex signature of Adrian *et al.* (2000*b*) and they are streamwise-aligned and inclined slightly away from the wall in the spirit of a hairpin packet. As in the channel-flow example, a retrograde vortex is noted in this realization and it appears to nest along the outer edge of the hairpin packet near prograde vortex C. In fact, the "nesting" of retrograde structures in the vicinity of clusters of prograde vortices in and around the log layer is commonly observed in the vast majority of instantaneous velocity realizations in both flows. This behavior is also clearly notable in the Λ_{ci} and local Galilean decomposition fields of figure 1.

Despite consistent observations of retrograde vortices nesting near prograde structures, it is impossible to infer the exact spatial relationships between these structures from instantaneous two-dimensional slices of the flow. This issue is further complicated by the fact that both flows are structurally-active, particularly within the log layer. For example, one might argue that spatially-coincident prograde and retrograde structures are in fact not isolated structures but instead form counter-rotating pairs in the spirit of Falco's typical eddy. This may indeed be the case; however, the present data does not allow for such a relationship to be confirmed and hence we can only report that retrograde structures often appear to cluster near prograde structures. Alternatively, the retrograde structures may actually be the by-product of the local dynamics of the hairpin vortices (as observed by Yang *et al.* (2001)) or the result of merging of hairpin structures as proposed by Tomkins & Adrian (2003). Nevertheless, as will be seen in section 5, even if every retrograde structure is directly related to a prograde vortex, streamwise-aligned prograde vortices with signatures consistent with hairpin structures still represent the majority of log-layer structure for the Re_τ range reported herein.

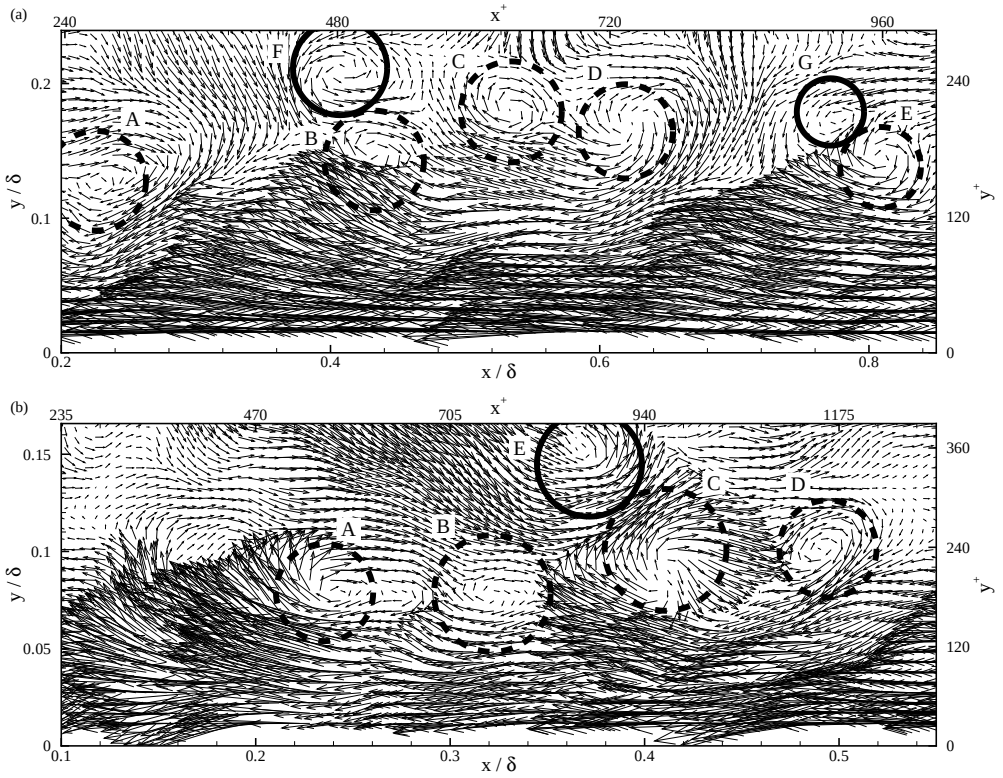

FIGURE 3. Examples of prograde and retrograde spanwise vortices via Galilean decomposition of instantaneous velocity fields in the streamwise–wall-normal plane of (a) turbulent channel flow at $\mathrm{Re}_\tau = 1185$ and (b) a turbulent boundary layer at $\mathrm{Re}_\tau = 2350$. Retrograde spanwise vortices are highlighted with solid circles; prograde vortices are highlighted with dashed circles.

5. Population trends and characteristics of the vortices

5.1. *Vortex population densities*

Since the spatial location of each vortex is assessed from the instantaneous Λ_{ci} fields, the population trends of both prograde and retrograde spanwise vortices can be studied as a function of wall-normal position and Reynolds number. The population density of prograde (retrograde) vortices, $\Pi_{p(r)}(y)$, is defined herein as the ensemble-averaged number of prograde (retrograde) spanwise vortices whose centers reside in rectangular areas of wall-normal height $3\Delta y/\delta$ and streamwise width L_x/δ centered at y, where L_x is the streamwise field of view for a given experiment. The use of an averaging window of height $3\Delta y/\delta$ minimizes scatter in the profiles, particularly at the lower Re_τ where the sample size tends to be small in the outer region. Therefore, $\Pi_{p(r)}(y)$ represents the average number of prograde (retrograde) spanwise vortices per δ^2 area at a given y location. Alternatively, $\Pi_{p(r)}^{-1}$ can be interpreted as the average outer-scaled area occupied by a prograde (retrograde) vortex at wall-normal position y.

Figure 4(a) presents Π_p as a function of y/δ for all channel and boundary-layer cases. The largest population densities of resolved prograde spanwise vortices are noted close to the wall ($y < 0.3\delta$), with Π_p monotonically decreasing with y in both flows and at all Re_τ. This behavior is similar to the instantaneous trends observed in figures 1 and 3 where the majority of prograde spanwise vortices reside in the region $y < 0.3\delta$. These wall-

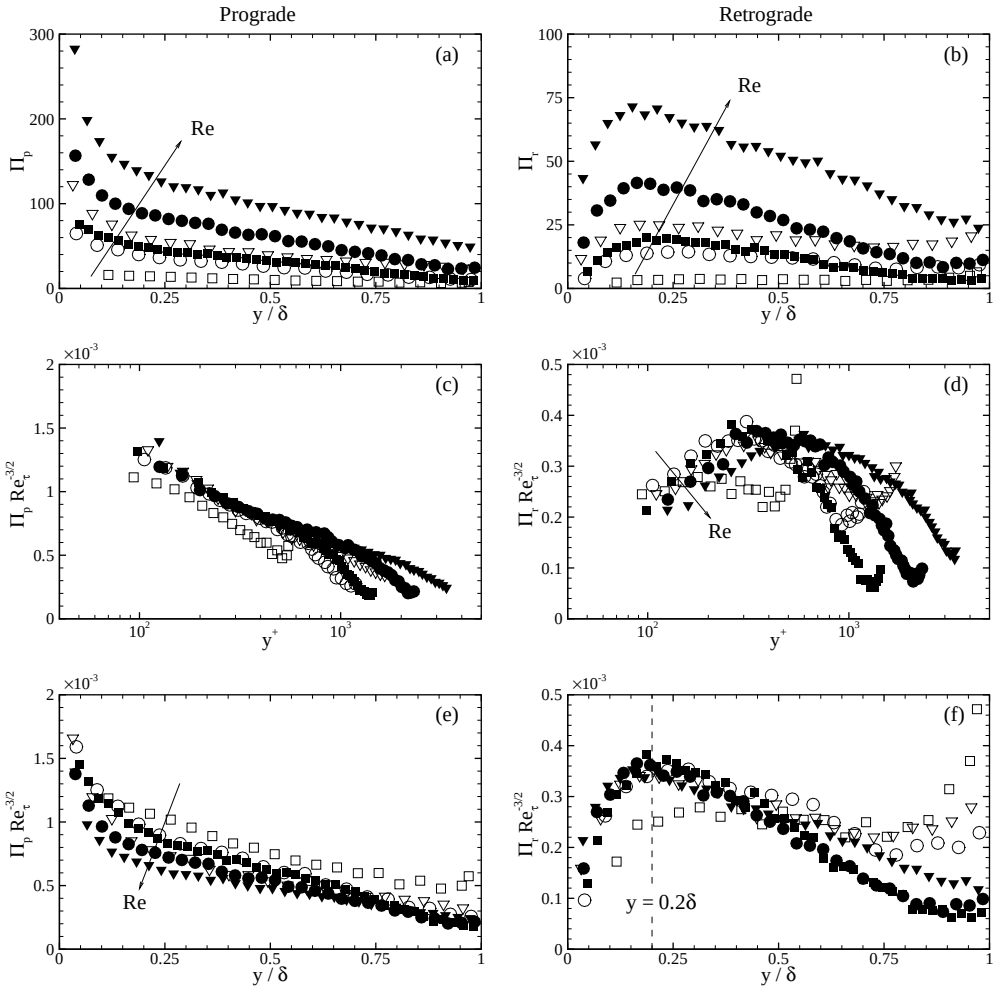

FIGURE 4. (a,b) Prograde and retrograde vortex population densities, Π_p and Π_r, versus y/δ. (c,d) Scaling of Π_p and Π_r with $\mathrm{Re}_\tau^{3/2}$ versus y^+. (e,f) Scaling of Π_p and Π_r with $\mathrm{Re}_\tau^{3/2}$ versus y/δ. Symbols are defined in table 1 and not all data points shown for clarity.

normal trends are consistent with the attached-eddy model of Perry & Chong (1982) and indicate that prograde spanwise vortices, many of which have structural characteristics consistent with the heads of hairpin vortices, may well originate very close to the wall. In addition, these wall-normal trends indicate that as prograde vortices grow away from the wall they may increase in average streamwise spacing as they advect downstream. This observation is supported by Christensen *et al.* (2004) who found that the average streamwise spacing of vortices within outer-layer vortex organization increases with y. For a fixed wall-normal position, Π_p increases with Re_τ in both flows. This trend is not surprising as their core sizes appear to have inner-scale dependence (Carlier & Stasnislas 2005). Therefore, a larger number of vortices per δ^2 area is possible with increasing Re_τ.

Alternatively, one may interpret the wall-normal trends of Π_p by noting that Π_p^{-1} represents the average outer-scaled area occupied by a prograde vortex. In this context, prograde vortices occupy a larger area in outer units, on average, with increasing wall-normal location. Note that this area does not represent the average area of the vortex

cores themselves but rather represents the space directly occupied by the cores and the empty space between adjacent cores (a "unit cell" of sorts). Therefore, an increase in the average area with wall-normal position need not imply that the actual core diameters of these structures increase appreciably with y. In fact, recent efforts indicate that their core diameters grow only slightly with y (Carlier & Stasnislas 2005). Rather, while it is probable that a portion of this trend can be explained by the dispersion of prograde structures as they grow away from the wall, it is also supportive of the merging mechanisms proposed in the attached-eddy model of Perry & Chong (1982) and the near-wall scale-growth observations and outer-layer merging scenarios of Tomkins & Adrian (2003).

Figure 4(b) presents the population densities of retrograde spanwise vortices, Π_r, as a function of y/δ for all channel and boundary-layer cases. In contrast to Π_p, Π_r grows steadily away from the wall to a local maximum near the outer edge of the log layer ($y \cong 0.2\delta$) in both flows and at all Re_τ. Beyond the log layer, Π_r decreases in both flows until approximately $y = 0.45\delta$ where Π_r continues to decrease in the boundary-layer cases. In the channel-flow cases, however, Π_r begins to increase again and reaches a magnitude at $y = \delta$ that is comparable to the Π_r peak near $y = 0.2\delta$. For fixed wall-normal position, Π_r increases with Re_τ in both flows, consistent with the Reynolds-number trends of Π_p. Therefore, while the channel and boundary-layer flows exhibit similar Π_p trends for all y, the Π_r trends differ considerably for $y > 0.45\delta$. These differences can be explained by noting that some fraction of the retrograde vortices in this region of channel flow may in fact have their origin from the flow along the opposing wall. Retrograde spanwise vortices in the reference frame of the bottom wall of the channel are equivalently prograde spanwise vortices in the reference frame of the top wall (since the y-coordinate is reflected about the centerline). Therefore, the increase in Π_r for $y \gtrsim 0.45\delta$ may be attributable to prograde vortices from the flow along the top wall of the channel, possibly hairpin structures, that have advected across the centerline and joined the flow along the bottom wall. The studies of Dean & Bradshaw (1976), Sabot & Compte-Bellot (1976) and Teitel & Antonia (1990), which show that the interaction region of turbulent channel flow has a wall-normal extent of $0.2\delta - 1.0\delta$ about the centerline, are supportive of this possibility.

Reynolds-number scaling of both Π_p and Π_r is also considered. Inner-scale dependence, $\Pi_{p(r)} \sim {\mathrm{Re}_\tau}^2$, was attempted since some evidence exists that the diameters of these spanwise structures scale with y_* (Carlier & Stasnislas 2005). However, profiles of $\Pi_p {\mathrm{Re}_\tau}^{-2}$ and $\Pi_r {\mathrm{Re}_\tau}^{-2}$ (not shown for brevity) exhibit clear Reynolds-number dependence when plotted versus y^+ and y/δ. In contrast, $\Pi_{p(r)} \sim {\mathrm{Re}_\tau}^{3/2}$ is found to be a more representative scaling of the population densities. This scaling is motivated by the Re_τ-dependence of the Kolmogorov length scale, η: $\delta/\eta \sim \mathrm{Re}_\tau^{3/4}$. As such, $\delta^2 \sim \eta^2 {\mathrm{Re}_\tau}^{3/2}$. Figure 4(c) presents profiles of $\Pi_p {\mathrm{Re}_\tau}^{-3/2}$ as a function of y^+ for all channel and boundary-layer cases. This Re_τ scaling yields collapse of Π_p in the region $100 < y^+ \lesssim 0.5\delta^+$ except for the $\mathrm{Re}_\tau = 570$ channel-flow case. While the wall-normal behavior of this low-Re case is consistent with the other Reynolds numbers, it does not collapse onto the other data in this scaling likely because it lacks an appreciable log layer. Apart from this low-Re deviation, Π_p exhibits clear $\mathrm{Re}_\tau^{3/2}$ dependence within the region $100 < y^+ < 0.5\delta^+$ for both flows, indicative of inner-layer dependence. In contrast, Figure 4(e) illustrates the Reynolds-number dependence of $\Pi_p {\mathrm{Re}_\tau}^{-3/2}$ when plotted versus y/δ.

Figure 4(d) presents $\Pi_r {\mathrm{Re}_\tau}^{-3/2}$ versus y^+ and Reynolds-number dependence is noted in the same wall-normal region where $\Pi_p {\mathrm{Re}_\tau}^{-3/2}$ collapses. In addition, the wall-normal position of the log-layer peak in Π_r grows with Re_τ when plotted on y^+. In contrast, $\Pi_r {\mathrm{Re}_\tau}^{-3/2}$ collapses in the region $y < 0.35\delta$ when plotted versus y/δ (figure 4(f)), including the peak value and position at $y = 0.2\delta$, save for the $\mathrm{Re}_\tau = 570$ channel-flow case.

This collapse on y/δ is indicative of outer-layer dependence. For $y > 0.35\delta$, the channel-flow cases deviate from the boundary-layer cases and Reynolds-number dependence is noted in both flows. Further, given that both the prograde and retrograde densities for the $\mathrm{Re}_\tau = 570$ channel-flow case fail to collapse on this scaling, this Reynolds number may not be sufficient for a mature structural state to exist.

Finally, since Π_p^{-1} and Π_r^{-1} can be interpreted as average unit areas occupied by prograde and retrograde vortices, respectively, these trends indicate that the characteristic areas occupied by prograde spanwise vortices in $100 < y^+ < 0.5\delta^+$ and retrograde structures for $y < 0.35\delta$ both have an Re_τ scaling consistent with that of η^2: $\mathrm{Re}_\tau^{-3/2}$. This behavior is consistent with the work of Morrison *et al.* (1992) who found that the average streamwise length of ω_z events, calculated from hot-wire data, scales as $\mathrm{Re}_\tau^{-3/4}$ ($\sim \eta$).

5.2. *Vortex population fractions*

One can recast the population trends of the prograde and retrograde spanwise vortices in terms of the proportion of these structures that reside at a given wall-normal location:

$$\Psi_r(y) \equiv \frac{\Pi_r(y)}{\Pi_p(y) + \Pi_r(y)}, \tag{5.1}$$

where Ψ_r is the fraction of retrograde spanwise vortices and $\Psi_p(y) = 1 - \Psi_r(y)$ represents the fraction of prograde spanwise vortices at a given wall-normal location. Plots of Ψ_r are presented in figures 5(a) and 5(b) for all three channel-flow Re_τ as a function of y^+ and y/δ, respectively (Ψ_p is not shown since $\Psi_p = 1 - \Psi_r$). When plotted versus y^+, Ψ_r displays similarity, within the scatter in the data, through $y^+ = 450$ for all three Re_τ, while the two higher Re_τ collapse through $y^+ = 950$. Note that $y^+ = 450$ at $\mathrm{Re}_\tau = 570$ and $y^+ = 950$ at $\mathrm{Re}_\tau = 1185$ both correspond to $y^+ = 0.8\delta^+$. This behavior indicates that the fraction of prograde and retrograde spanwise vortices exhibit similarity in channel flow through nearly the entire outer region versus y^+ for the Re_τ range reported. Similar collapse is not noted when Ψ_r is plotted versus y/δ, although a region of relative constancy for fixed Re_τ is observed between $0.25 < y/\delta < 0.75$ where the proportion of retrograde spanwise vortices increases slightly with Re_τ. For example, at $\mathrm{Re}_\tau = 570$, 20–25% of the spanwise vortices are retrograde, while at $\mathrm{Re}_\tau = 1760$, 25–30% are retrograde. The retrograde fractions converge to 0.5 at all three Re_τ as the centerline is approached, consistent with the symmetry of channel flow about its centerline.

Figures 5(c) and 5(d) present Ψ_r at all three boundary-layer Re_τ versus y^+ and y/δ, respectively. In contrast to the channel-flow retrograde fractions, Ψ_r for the boundary-layer cases exhibits similarity for a reduced y^+ range, with the $\mathrm{Re}_\tau = 1400$ fraction departing this collapse near $y^+ = 420$ and the $\mathrm{Re}_\tau = 2350$ fraction departing near $y^+ = 700$. These points of departure both correspond to $y^+ = 0.3\delta^+$, indicating that similarity in Ψ_p and Ψ_r does not extend beyond the log layer of the turbulent boundary layer. When plotted versus y/δ, Ψ_r decreases slowly in the region $0.25 < y/\delta < 0.75$ of the boundary layer, in stark contrast to the channel-flow behavior noted in the same region. Nevertheless, the Reynolds-number dependence of Ψ_r in the boundary layer is consistent with channel flow: Ψ_r increases slightly with Re_τ.

Figures 5(e) and 5(f) show overlays of Ψ_r from the channel and boundary-layer cases versus y^+ and y/δ, respectively. The retrograde fractions collapse along a similar path, within the scatter of the data, irrespective of flow and Re_τ for $100 < y^+ < 0.3\delta^+$ when plotted versus y^+, beyond which the boundary-layer cases depart from this similarity. The slight scatter that exists between the boundary-layer and channel-flow data is well within the error bounds of using the Clauser chart method to determine u_* and y_* for the boundary-layer experiments and could also be associated with the fact that the boundary-

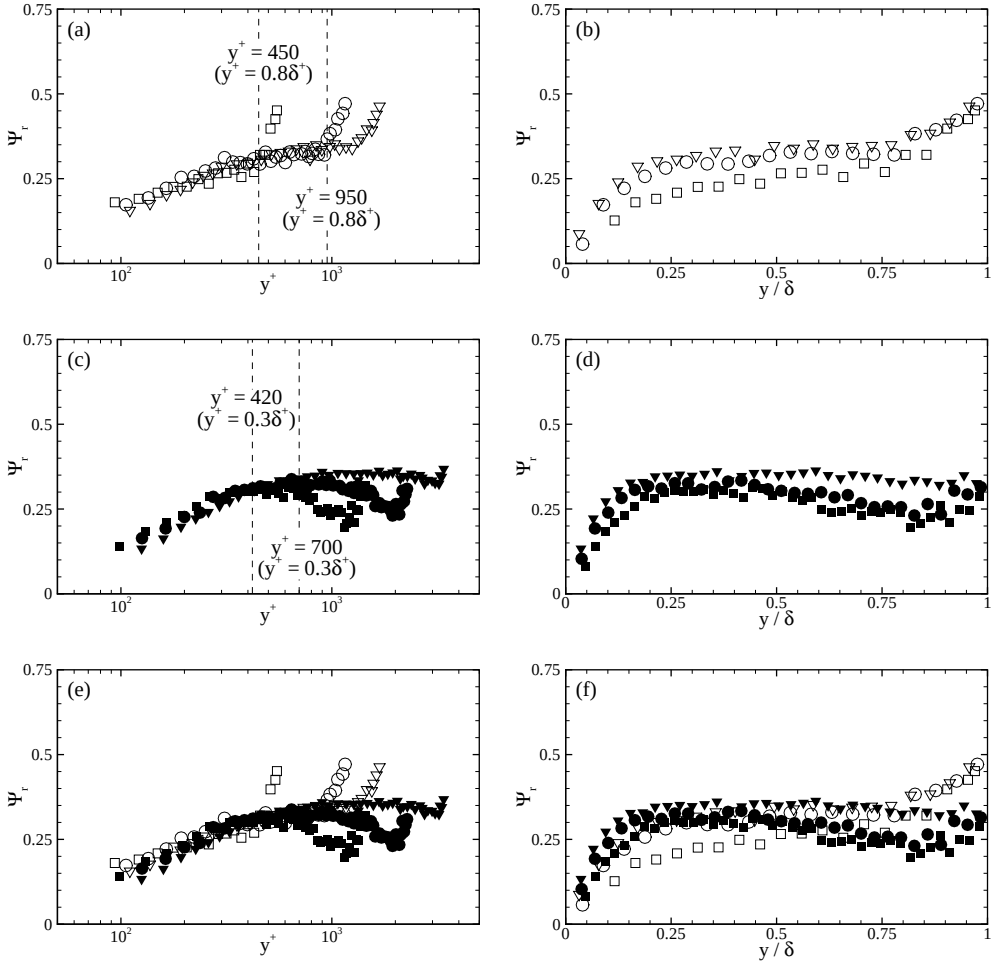

FIGURE 5. Fraction of retrograde (Ψ_r) spanwise vortices in (a,b) turbulent channel flow and (c,d) a turbulent boundary layer versus y^+ and y/δ, respectively. (e,f) Overlay of Ψ_r from both flows. Symbols are defined in table 1 and not all data points shown for clarity.

layer data is slightly less resolved in inner units ($11y_*$ versus $9y_*$ (channel)). Nevertheless, a clear consistency in Ψ_r exists between the two flows in the region $100 < y^+ < 0.3\delta^+$. The channel and boundary-layer retrograde fractions display Re_τ dependence when plotted versus y/δ, with the $\mathrm{Re}_\tau = 3450$ boundary-layer data having the largest values of Ψ_r and the $\mathrm{Re}_\tau = 570$ channel data displaying the smallest. Therefore, these trends indicate that the prevalence of prograde, most-likely hairpin, structures outside the log layer decreases slightly with increasing Reynolds number. However, it is also observed that the growth rate of Ψ_r with Reynolds number appears to slow slightly at higher Re_τ, meaning constant values of Ψ_r and Ψ_p may eventually be attained. Unfortunately, the Re_τ range presented is not sufficient to draw conclusions in this regard.

5.3. *Fixed Re_τ channel and boundary-layer population trends*

The similarities and differences between channel and boundary-layer flows can be further assessed by contrasting the population trends of prograde and retrograde spanwise

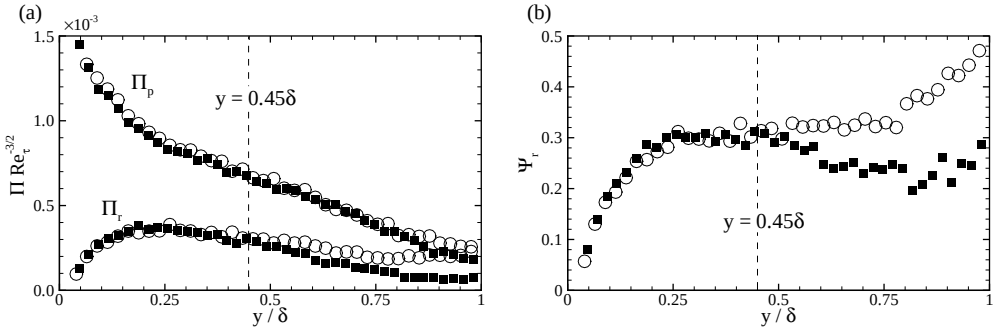

FIGURE 6. Comparison of channel flow ($\mathrm{Re}_\tau = 1185$) and boundary layer ($\mathrm{Re}_\tau = 1400$) (a) population densities (Π_p and Π_r) and (b) retrograde vortex fractions (Ψ_r). Symbols are defined in table 1 and not all data points shown for clarity.

vortices at two nearly-identical Re_τ in each flow. Figure 6(a) presents Π_p and Π_r for the $\mathrm{Re}_\tau = 1185$ channel and $\mathrm{Re}_\tau = 1400$ boundary-layer cases. The prograde population densities are nearly identical for all wall-normal locations save for some deviation near $y = \delta$. In contrast, the retrograde population densities collapse for $y < 0.45\delta$, beyond which Π_r continues to decrease in the boundary layer while increasing again near $y = \delta$ in channel flow. These differences in Π_r for $y > 0.45\delta$ are therefore responsible for deviations noted in the fraction of retrograde vortices, Ψ_r, of the channel and boundary-layer cases (figure 6(b)). As was noted earlier, the increase in Π_r and Ψ_r near the centerline of channel flow is most-likely due to prograde structures in the reference frame of the top wall that have crossed the centerline to join the flow along the bottom wall as retrograde structures. Based on similar arguments, one might expect a deficit of prograde vortices in channel flow near $y = \delta$, compared to the boundary layer, since presumably some of the prograde structures in the reference frame of the bottom wall cross the centerline to join the flow along the top wall. However, the prograde populations near $y = \delta$ can also be enhanced by retrograde structures in the reference frame of the top wall that may cross the centerline and join the flow along the bottom wall. This cross-population of structures across the centerline would account for the slightly larger values of Π_p near $y = \delta$ in channel flow compared to the boundary layer. Nevertheless, the noted consistency in Π_p, Π_r and Ψ_r for $y < 0.45\delta$ indicates that the structural features of these flows are essentially the same in the lower half of both flows. As such, the present results suggest that the region $\pm 0.55\delta$ about the centerline can be regarded as a region where structures from both walls coexist. This estimate of the interaction region is larger than that cited by Dean & Bradshaw (1976) ($\pm 0.2\delta$) and Sabot & Compte-Bellot (1976) ($\pm 0.3\delta$) but smaller than the observations of Teitel & Antonia (1990) which indicated that events originating at one wall can often reach the inner layer of the opposing wall.

5.4. *Contributions to mean shear*

The contributions of prograde and retrograde spanwise vortices to the overall mean shear are also assessed from the PIV ensembles. The total mean shear in wall turbulence is given by

$$\tau(y) = \mu \frac{\partial U}{\partial y} - \rho \langle u' v' \rangle, \tag{5.2}$$

where the first term on the right-hand side represents the mean viscous shear and the second term embodies the shear contributions due to turbulent stresses (primes denote fluctuating quantities). The contributions of prograde (retrograde) spanwise vortex cores

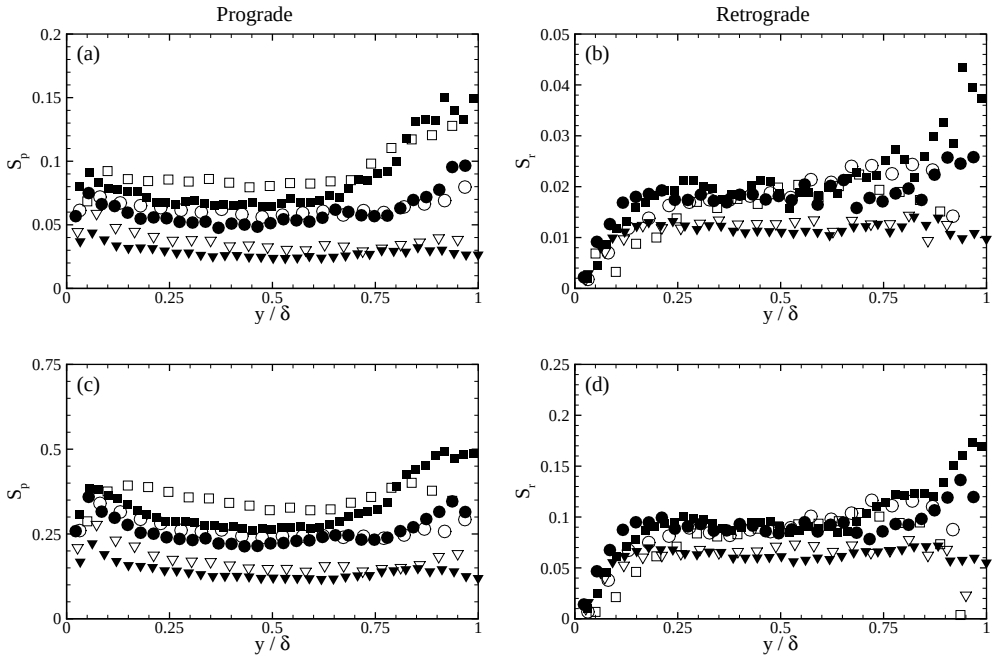

FIGURE 7. (a,b) Fraction of mean shear contained within prograde and retrograde vortex cores, respectively. (c,d) Fraction of mean shear associated with cores and locally-induced motions for prograde and retrograde structures, respectively. Symbols are defined in table 1 and not all data points shown for clarity.

to $\tau(y)$ can be computed as a stress fraction of the form

$$S_{p(r)}(y) \equiv \frac{\tau_{p(r)}(y)}{\tau(y)}, \tag{5.3}$$

where $\tau_{p(r)}$ represents the mean shear contained within the cores of prograde (retrograde) vortices at a given y. These stress fractions represent lower bounds on the mean-shear contributions of these structures since they only account for the mean shear contained *within* the cores themselves and not any shear induced by the vortex cores.

Figure 7(a) presents the mean-shear contributions of prograde spanwise vortex cores, S_p, as a function of wall-normal position for both the channel and boundary-layer datasets. The contributions reach a local maximum close to the wall for fixed Re_τ and decline slightly to a region of relative constancy for $0.25 < y/\delta < 0.75$, beyond which they increase again. The peak in prograde mean-shear contributions close to the wall is coincident with the largest populations of prograde spanwise vortices as noted earlier (figure 4). In addition, a clear Reynolds-number trend is evident, particularly within the region of constancy, with prograde structures contributing a larger fraction to the mean shear at lower Re_τ (8–9% for the $\mathrm{Re}_\tau = 570$ channel-flow case compared to 3–4% for the $\mathrm{Re}_\tau = 3450$ boundary-layer case). In contrast, the retrograde vortex cores contribute very little to the mean shear (figure 7(b)), particularly close to the wall where their contributions are less than 1% over the Re_τ range reported herein. The retrograde mean-shear contributions reach a maximum of 1–2% near $y = 0.2\delta$, consistent with the log-layer peak in their population densities. As with the prograde contributions, the retrograde mean-shear contributions attain a region of relative constancy for $0.25 < y/\delta < 0.75$ and decrease slightly with increasing Reynolds number.

While the prograde and retrograde vortex cores contribute little to the overall mean shear, the instantaneous realizations presented herein suggest that the motions induced by these cores can generate significant instantaneous shear. Therefore, the mean-shear contributions of both the cores and the induced-motions in the immediate vicinity of the cores are estimated by centering a bounding box about each vortex core with sides two grid-points larger than the extent of the vortex core in each direction as determined by the $|\widetilde{\Lambda}_{ci}| \geqslant 1.5$ threshold. Care is taken to ensure that these induced motions are included only once in the calculation as it is possible that the bounding box of one vortex may overlap that of a neighboring vortex. These core and induced-flow mean-shear contributions are presented in figures 7(c) and 7(d) for prograde and retrograde vortices, respectively. While their qualitative wall-normal and Reynolds-number trends are identical to those observed for the core contributions alone, inclusion of the induced motions in the immediate vicinity of the cores increases the mean-shear contributions by a factor of 4–5 for both retrograde and prograde vortices. Therefore, while the vortex cores themselves contribute very little to the overall mean shear, the motions induced by these structures can generate significant shear.

5.5. *Advection velocities*

Since the location of each spanwise vortex is identified in the present effort, the instantaneous streamwise advection velocities of the vortices can also be assessed. Figures 8(a) and 8(b) present the mean advection velocities, U_c, of both prograde and retrograde spanwise vortices as a function of wall-normal position for the $\mathrm{Re}_\tau = 1760$ channel-flow and $\mathrm{Re}_\tau = 2350$ boundary-layer cases, respectively (For brevity, only these two Reynolds numbers are presented as the other channel and boundary-layer cases exhibit similar trends). On average, both prograde and retrograde spanwise vortices advect with the mean streamwise velocity in both flows, consistent with the recent log-layer results of Carlier & Stasnislas (2005) (although they did not differentiate between the advection velocities of prograde and retrograde structures). However, while the mean advection velocities of these vortices collapse on the local streamwise mean, the distributions of advection velocities about the mean exhibit strong wall-normal dependence. Histograms of the prograde and retrograde advection velocities at three different wall-normal locations are presented in figures 8(c–e) for the channel-flow case and figures 8(f–h) for the boundary-layer case. These histograms have broad widths at the inner boundary of the log layer, with some prograde and retrograde structures advecting as much as 30% faster or slower than the local mean in both flows. The widths of the histograms decrease slightly with increasing y but are still relatively broad even at the outer edge of the log layer. Farther away from the wall at $y = 0.75\delta$, the histograms become much narrower with most of the structures advecting within 10% of the local streamwise mean. Interestingly, the widths of the histograms are found to be proportional to the local RMS streamwise velocity, σ_u. Therefore, while both prograde and retrograde spanwise vortices travel on average with the local mean velocity, their instantaneous advection velocities are strongly influenced by the local turbulence levels, particularly close to the wall.

6. Conclusions

The results presented show that prograde and retrograde spanwise vortices occur frequently throughout both turbulent channel flow and the zero-pressure-gradient turbulent boundary layer, with the largest populations existing in the region $100 < y^+ < 0.25\delta^+$: the log layer. In particular, the inner boundary of the log layer in both channel and boundary-layer flows is densely populated by prograde spanwise vortices that bear char-

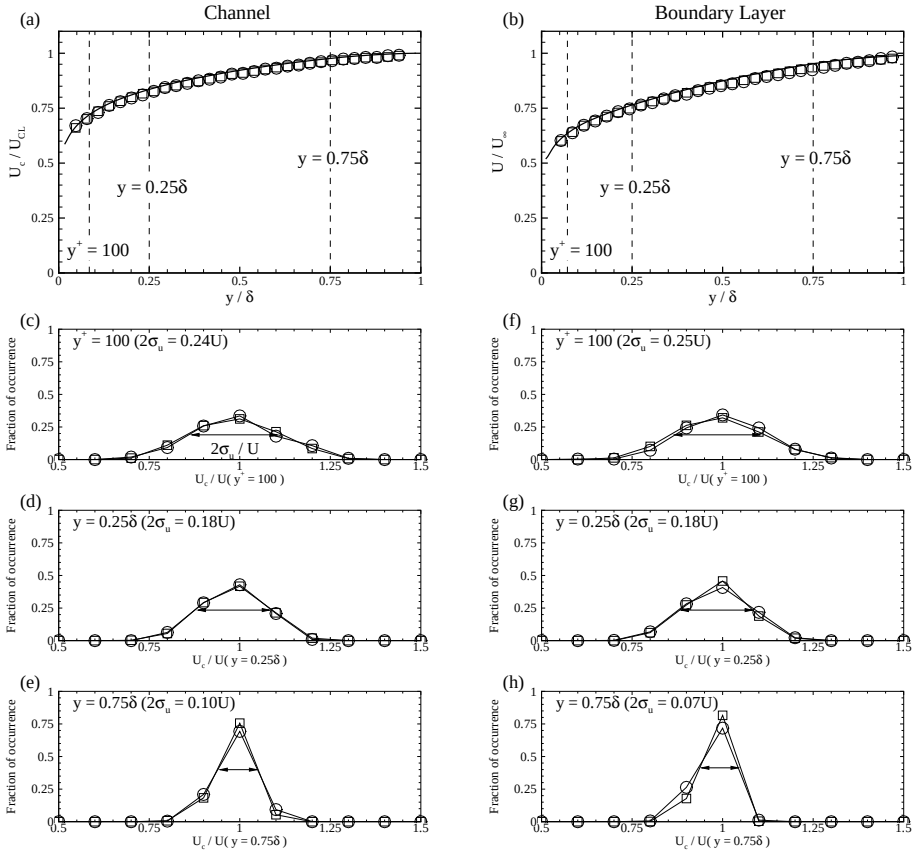

FIGURE 8. Mean advection velocities of prograde and retrograde spanwise vortices versus y/δ in (a) turbulent channel flow at $\mathrm{Re}_\tau = 1760$ and (b) a turbulent boundary layer at $\mathrm{Re}_\tau = 2350$. Solid lines represent the mean velocity profiles. (c)–(e) Histograms of prograde and retrograde vortex advection velocities at $y^+ = 100$, $y = 0.25\delta$ and $y = 0.75\delta$ for case shown in (a); (f)–(h) Histograms of prograde and retrograde vortex advection velocities at $y^+ = 100$, $y = 0.25\delta$ and $y = 0.75\delta$ for case shown in (b). Arrows in (c–h) represent the $2\sigma_u$ width of pdf's for each wall-normal location. □: Prograde; ○: Retrograde.

acteristics consistent with the heads of hairpin vortices, the building-blocks of outer-layer vortex organization (Adrian *et al.* 2000*b*). The log layer is also populated by many retrograde spanwise vortices, with their maximum populations occurring near the outer edge of the log layer ($y \cong 0.2\delta$) in both turbulent channel and boundary-layer flows. While their origin cannot be inferred from instantaneous two-dimensional snapshots of the flow, these retrograde structures accumulate near the outer edge of the log layer and are often observed to nest near clusters of prograde vortices that form hairpin vortex packets. However, while both channel flow and the boundary layer show identical retrograde-vortex population trends in the log layer, these flows differ considerably in this regard for $y > 0.45\delta$. In particular, both the population density and fraction of retrograde vortices decrease with wall-normal position beyond the log layer in the boundary layer while these quantities increase with y in channel flow near its centerline. Such differences are likely associated with the influence of the opposing wall in channel flow whereby prograde structures in the reference frame of the top wall appear as retrograde vortices in the reference frame of the bottom wall. Therefore, the region $\pm 0.55\delta$ about the center-

line of channel flow can be regarded as an interaction region where structures from both walls commonly exist. Nevertheless, the structural populations of channel flow and the boundary layer are found to be the same below this interaction region for similar Re_τ.

The population densities of resolved prograde vortices show $\mathrm{Re}_\tau^{3/2}$ dependence in both flows when plotted versus y^+ for $100 < y^+ < 0.5\delta^+$, consistent with a Kolmogorov-type scaling ($\delta^2/\eta^2 \sim {\mathrm{Re}_\tau}^{3/2}$) and indicative of inner-layer dependence. The population densities of resolved retrograde structures are found to collapse with the same scaling when plotted versus y/δ for $y < 0.35\delta$, indicative of outer-layer dependence. These scalings suggests that the characteristic areas occupied by prograde and retrograde vortices in the regions of collapse scale with η^2. When the population densities are recast in terms of fractions of prograde and retrograde structures, similarity is noted within the log layer when plotted versus y^+. This behavior is found to be flow-independent, as the results from both channel flow and the boundary layer collapse along the same path for $100 < y^+ < 0.3\delta^+$. In addition, the proportion of retrograde spanwise vortices grows slightly with Re_τ in both flows for $y > 0.25\delta$, indicating that retrograde structures may play an increasingly important role at higher Reynolds numbers.

Finally, prograde and retrograde cores travel, on average, with the local mean velocity, although their instantaneous advection velocities can be significantly altered by the local turbulence levels. In addition, prograde and retrograde cores contribute very little to the overall mean shear. However, the motions induced by these vortices do make significant contributions in this regard, particularly in the case of prograde structures which can contribute between 20 and 40% (with larger contributions occurring at lower Re_τ).

The channel-flow experiments were performed during the second author's tenure at the University of New Mexico with funding from Oak Ridge Associated Universities via a Junior Faculty Enhancement Award. The boundary-layer work was performed at the University of Illinois with funding from the Air Force Office of Scientific Research under Grants FA9550-05-1-0043 and FA9550-05-1-0246 (Dr. Rhett Jeffries, Program Manager).

REFERENCES

Adrian, R. J., Christensen, K. T. & Liu, Z.-C. 2000*a* Analysis and interpretation of instantaneous turbulent velocity fields. *Exp. Fluids* **29**, 275–290.

Adrian, R. J., Meinhart, C. D. & Tomkins, C. D. 2000*b* Vortex organization in the outer region of the turbulent boundary layer. *J. Fluid Mech.* **422**, 1–54.

Brooke, J. W. & Hanratty, T. J. 1993 Origin of turbulence-producing eddies in a channel flow. *Phys. Fluids* **5** (4), 1011–1022.

Carlier, J. & Stasnislas, M. 2005 Experimental study of eddy structures in a turbulent boundary layer using particle image velocimetry. *J. Fluid Mech.* **535**, 143–188.

Chakraborty, P., Balachandar, S. & Adrian, R. J. 2005 On the relationships between local vortex identification schemes. *J. Fluid Mech.* **535**, 189–214.

Chong, M. S., Perry, A. E. & Cantwell, B. J. 1990 A general classification of three-dimensional flow fields. *Phys. Fluids* **2** (5), 765–777.

Christensen, K. T., Wu, Y., Adrian, R. J. & Lai, W. 2004 Statistical imprints of structure in wall turbulence AIAA Paper 2004-1116.

Dean, R. B. & Bradshaw, P. 1976 Measurements of interacting turbulent shear layers in a duct. *J. Fluid Mech.* **78**, 641–676.

Delo, C. J., Kelso, R. M. & Smits, A. J. 2004 Three-dimensional structure of a low-Reynolds-number turbulent boundary layer. *J. Fluid Mech.* **512**, 47–83.

Falco, R. E. 1977 Coherent motions in the outer region of turbulent boundary layers. *Phys. Fluids* **20** (10), S124–S132.

Falco, R. E. 1983 New results, a review and synthesis of the mechanism of turbulence production in boundary layers and its modification. In *AIAA Paper 83-0377*.

Falco, R. E. 1991 A coherent structure model of the turbulent boundary layer and its ability to predict Reynolds number dependence. *Phil. Trans. R. Soc. Lond. A* **336**, 103–129.

Ganapathisubramani, B., Longmire, E. K. & Marusic, I. 2003 Characteristics of vortex packets in turbulent boundary layers. *J. Fluid Mech.* **478**, 35–46.

Head, M. R. & Bandyopadhyay, P. 1981 New aspects of turbulent boundary-layer structure. *J. Fluid Mech.* **107**, 297–338.

Klewicki, J. C. 1997 Self-sustaining traits of near-wall motions underlying boundary layer stress transport. In *Self-Sustaining Mechanisms of Wall Turbulence* (ed. R. L. Panton), chap. 7, pp. 135–166. Computational Mechanics Publications.

Klewicki, J. C., Gendrich, C. P., Foss, J. F. & Falco, R. E. 1990 On the sign of the instantaneous spanwise vorticity component in the near-wall region of turbulent boundary layers. *Phys. Fluids* **2** (8), 1497–1500.

Klewicki, J. C. & Hirschi, C. R. 2004 Flow field properties local to near-wall shear layers in a low Reynolds number turbulent boundary layer. *Phys. Fluids* **16** (11), 4163–4176.

Kline, S. J. & Robinson, S. K. 1989 Quasi-coherent structures in the turbulent boundary layer. Part 1: Status report on a community-wide summary of the data. In *Near Wall Turbulence* (ed. S. J. Kline & N. H. Afgan), pp. 218–247. Hemisphere.

Liu, Z.-C., Adrian, R. J. & Haratty, T. J. 2001 Large-scale modes of turbulent channel flow: Transport and structure. *J. Fluid Mech.* **448**, 53–80.

Marusic, I. 2001 On the role of large-scale structures in wall turbulence. *Phys. Fluids* **13** (3), 735–743.

Meinhart, C. D. 1994 Investigation of turbulent boundary-layer structure using particle-image velocimetry. PhD thesis, Department of Theoretical and Applied Mechanics, University of Illinois at Urbana-Champaign, Urbana, Ill.

Melander, M. V. & Zabuski, N. J. 1988 Interaction and apparent reconnection of 3D vortex tubes via direct numerical simulations. *Fluid Dynamics Res.* **3**, 247–250.

Moin, P., Leonard, A. & Kim, J. 1986 Evolution of a curved vortex filament into a vortex ring. *Phys. Fluids* **29**, 955–963.

Morrison, J. F., Subramanian, C. S. & Bradshaw, P. 1992 Bursts and the law of the wall in turbulent boundary layers. *J. Fluid Mech.* **241**, 75–108.

Nagaosa, R. & Handler, R. A. 2003 Statistical analysis of coherent vortices near a free surface in a fully developed turbulence. *Phys. Fluids* **15** (2), 375–394.

Perry, A. E. & Chong, M. S. 1982 On the mechanism of wall turbulence. *J. Fluid Mech.* **119**, 173–217.

Perry, A. E. & Marusic, I. 1995 A wall-wake model for the turbulence structure of boundary layers. part 1. extension of the attached eddy hypothesis. *J. Fluid Mech.* **298**, 361–388.

Sabot, J. & Compte-Bellot, G. 1976 Intermittency of coherent structures in the core region of fully developed turbulent pipe flow. *J. Fluid Mech.* **74**, 767–796.

Schoppa, W. & Hussain, F. 1997 Genesis and dynamics of coherent structures in near-wall turbulence: A new look. In *Self-Sustaining Mechanisms of Wall Turbulence* (ed. R. L. Panton), chap. 16, pp. 385–422. Computational Mechanics Publications.

Smith, C. R. 1984 A synthesized model of the near-wall behavior in turbulent boundary layers. In *Proceedings of the* 8^{th} *Symposium on Turbulence*, pp. 299–325. Univ. Missouri-Rolla, Rolla, Missouri.

Smith, C. R., Walker, J. D. A., Haidari, A. H. & Sobrun, U. 1991 On the dynamics of near-wall turbulence. *Philosophical Transactions of the Royal Society of London A* **336**, 131–175.

Teitel, M. & Antonia, R. A. 1990 The interaction region of a turbulent duct flow. *Phys. Fluids* **2** (5), 808–813.

Theodorsen, T. 1952 Mechanism of turbulence. In *Proceedings of the 2nd Midwestern Conference on Fluid Mechanics*, pp. 1–19. Ohio State University, Columbus, Ohio.

Tomkins, C. D. & Adrian, R. J. 2003 Spanwise structure and scale growth in turbulent boundary layers. *J. Fluid Mech.* **490**, 37–74.

Yang, M., Meng, H. & Sheng, J. 2001 Dynamics of hairpin vortices generated by a mixing tab in a channel flow. *Exp. Fluids* **30**, 705–722.

Zhou, J., Adrian, R. J., Balachandar, S. & Kendall, T. M. 1999 Mechanisms for generating coherent packets of hairpin vortices in channel flow. *J. Fluid Mech.* **387**, 353–396.

List of Recent TAM Reports

No.	*Authors*	*Title*	*Date*
1000	Kessler, M. R., and S. R. White	Cure kinetics of ring-opening metathesis polymerization of dicyclopentadiene—*Journal of Polymer Science A* **40**, 2373–2383 (2002)	Feb. 2002
1001	Dolbow, J. E., E. Fried, and A. Q. Shen	Point defects in nematic gels: The case for hedgehogs—*Archive for Rational Mechanics and Analysis* **177**, 21–51 (2005)	Feb. 2002
1002	Riahi, D. N.	Nonlinear steady convection in rotating mushy layers—*Journal of Fluid Mechanics* **485**, 279–306 (2003)	Mar. 2002
1003	Carlson, D. E., E. Fried, and S. Sellers	The totality of soft-states in a neo-classical nematic elastomer—*Journal of Elasticity* **69**, 169–180 (2003) with revised title	Mar. 2002
1004	Fried, E., and R. E. Todres	Normal-stress differences and the detection of disclinations in nematic elastomers—*Journal of Polymer Science B: Polymer Physics* **40**, 2098–2106 (2002)	June 2002
1005	Fried, E., and B. C. Roy	Gravity-induced segregation of cohesionless granular mixtures—*Lecture Notes in Mechanics*, in press (2002)	July 2002
1006	Tomkins, C. D., and R. J. Adrian	Spanwise structure and scale growth in turbulent boundary layers—*Journal of Fluid Mechanics* (submitted)	Aug. 2002
1007	Riahi, D. N.	On nonlinear convection in mushy layers: Part 2. Mixed oscillatory and stationary modes of convection—*Journal of Fluid Mechanics* **517**, 71–102 (2004)	Sept. 2002
1008	Aref, H., P. K. Newton, M. A. Stremler, T. Tokieda, and D. L. Vainchtein	Vortex crystals—*Advances in Applied Mathematics* **39**, in press (2002)	Oct. 2002
1009	Bagchi, P., and S. Balachandar	Effect of turbulence on the drag and lift of a particle—*Physics of Fluids*, in press (2003)	Oct. 2002
1010	Zhang, S., R. Panat, and K. J. Hsia	Influence of surface morphology on the adhesive strength of aluminum/epoxy interfaces—*Journal of Adhesion Science and Technology* **17**, 1685–1711 (2003)	Oct. 2002
1011	Carlson, D. E., E. Fried, and D. A. Tortorelli	On internal constraints in continuum mechanics—*Journal of Elasticity* **70**, 101–109 (2003)	Oct. 2002
1012	Boyland, P. L., M. A. Stremler, and H. Aref	Topological fluid mechanics of point vortex motions—*Physica D* **175**, 69–95 (2002)	Oct. 2002
1013	Bhattacharjee, P., and D. N. Riahi	Computational studies of the effect of rotation on convection during protein crystallization—*International Journal of Mathematical Sciences* **3**, 429–450 (2004)	Feb. 2003
1014	Brown, E. N., M. R. Kessler, N. R. Sottos, and S. R. White	*In situ* poly(urea-formaldehyde) microencapsulation of dicyclopentadiene—*Journal of Microencapsulation* (submitted)	Feb. 2003
1015	Brown, E. N., S. R. White, and N. R. Sottos	Microcapsule induced toughening in a self-healing polymer composite—*Journal of Materials Science* (submitted)	Feb. 2003
1016	Kuznetsov, I. R., and D. S. Stewart	Burning rate of energetic materials with thermal expansion—*Combustion and Flame* (submitted)	Mar. 2003
1017	Dolbow, J., E. Fried, and H. Ji	Chemically induced swelling of hydrogels—*Journal of the Mechanics and Physics of Solids*, in press (2003)	Mar. 2003
1018	Costello, G. A.	Mechanics of wire rope—Mordica Lecture, Interwire 2003, Wire Association International, Atlanta, Georgia, May 12, 2003	Mar. 2003
1019	Wang, J., N. R. Sottos, and R. L. Weaver	Thin film adhesion measurement by laser induced stress waves—*Journal of the Mechanics and Physics of Solids* (submitted)	Apr. 2003
1020	Bhattacharjee, P., and D. N. Riahi	Effect of rotation on surface tension driven flow during protein crystallization—*Microgravity Science and Technology* **14**, 36–44 (2003)	Apr. 2003
1021	Fried, E.	The configurational and standard force balances are not always statements of a single law—*Proceedings of the Royal Society* (submitted)	Apr. 2003

List of Recent TAM Reports (cont'd)

No.	*Authors*	*Title*	*Date*
1022	Panat, R. P., and K. J. Hsia	Experimental investigation of the bond coat rumpling instability under isothermal and cyclic thermal histories in thermal barrier systems—*Proceedings of the Royal Society of London A* **460**, 1957–1979 (2003)	May 2003
1023	Fried, E., and M. E. Gurtin	A unified treatment of evolving interfaces accounting for small deformations and atomic transport: grain-boundaries, phase transitions, epitaxy—*Advances in Applied Mechanics* **40**, 1–177 (2004)	May 2003
1024	Dong, F., D. N. Riahi, and A. T. Hsui	On similarity waves in compacting media—*Horizons in World Physics* **244**, 45–82 (2004)	May 2003
1025	Liu, M., and K. J. Hsia	Locking of electric field induced non-180° domain switching and phase transition in ferroelectric materials upon cyclic electric fatigue—*Applied Physics Letters* **83**, 3978–3980 (2003)	May 2003
1026	Liu, M., K. J. Hsia, and M. Sardela Jr.	In situ X-ray diffraction study of electric field induced domain switching and phase transition in PZT-5H—*Journal of the American Ceramics Society* (submitted)	May 2003
1027	Riahi, D. N.	On flow of binary alloys during crystal growth—*Recent Research Development in Crystal Growth* **3**, 49–59 (2003)	May 2003
1028	Riahi, D. N.	On fluid dynamics during crystallization—*Recent Research Development in Fluid Dynamics* **4**, 87–94 (2003)	July 2003
1029	Fried, E., V. Korchagin, and R. E. Todres	Biaxial disclinated states in nematic elastomers—*Journal of Chemical Physics* **119**, 13170–13179 (2003)	July 2003
1030	Sharp, K. V., and R. J. Adrian	Transition from laminar to turbulent flow in liquid filled microtubes—*Physics of Fluids* (submitted)	July 2003
1031	Yoon, H. S., D. F. Hill, S. Balachandar, R. J. Adrian, and M. Y. Ha	Reynolds number scaling of flow in a Rushton turbine stirred tank: Part I—Mean flow, circular jet and tip vortex scaling—*Chemical Engineering Science* (submitted)	Aug. 2003
1032	Raju, R., S. Balachandar, D. F. Hill, and R. J. Adrian	Reynolds number scaling of flow in a Rushton turbine stirred tank: Part II—Eigen-decomposition of fluctuation—*Chemical Engineering Science* (submitted)	Aug. 2003
1033	Hill, K. M., G. Gioia, and V. V. Tota	Structure and kinematics in dense free-surface granular flow—*Physical Review Letters* **91**, 064302 (2003)	Aug. 2003
1034	Fried, E., and S. Sellers	Free-energy density functions for nematic elastomers—*Journal of the Mechanics and Physics of Solids* **52**, 1671–1689 (2004)	Sept. 2003
1035	Kasimov, A. R., and D. S. Stewart	On the dynamics of self-sustained one-dimensional detonations: A numerical study in the shock-attached frame—*Physics of Fluids* (submitted)	Nov. 2003
1036	Fried, E., and B. C. Roy	Disclinations in a homogeneously deformed nematic elastomer—*Nature Materials* (submitted)	Nov. 2003
1037	Fried, E., and M. E. Gurtin	The unifying nature of the configurational force balance—*Mechanics of Material Forces* (P. Steinmann and G. A. Maugin, eds.), in press (2003)	Dec. 2003
1038	Panat, R., K. J. Hsia, and J. W. Oldham	Rumpling instability in thermal barrier systems under isothermal conditions in vacuum—*Philosophical Magazine*, in press (2004)	Dec. 2003
1039	Cermelli, P., E. Fried, and M. E. Gurtin	Sharp-interface nematic–isotropic phase transitions without flow—*Archive for Rational Mechanics and Analysis* **174**, 151–178 (2004)	Dec. 2003
1040	Yoo, S., and D. S. Stewart	A hybrid level-set method in two and three dimensions for modeling detonation and combustion problems in complex geometries—*Combustion Theory and Modeling* (submitted)	Feb. 2004
1041	Dienberg, C. E., S. E. Ott-Monsivais, J. L. Ranchero, A. A. Rzeszutko, and C. L. Winter	Proceedings of the Fifth Annual Research Conference in Mechanics (April 2003), TAM Department, UIUC (E. N. Brown, ed.)	Feb. 2004

List of Recent TAM Reports (cont'd)

No.	Authors	Title	Date
1042	Kasimov, A. R., and D. S. Stewart	Asymptotic theory of ignition and failure of self-sustained detonations—*Journal of Fluid Mechanics* (submitted)	Feb. 2004
1043	Kasimov, A. R., and D. S. Stewart	Theory of direct initiation of gaseous detonations and comparison with experiment—*Proceedings of the Combustion Institute* (submitted)	Mar. 2004
1044	Panat, R., K. J. Hsia, and D. G. Cahill	Evolution of surface waviness in thin films via volume and surface diffusion—*Journal of Applied Physics* (submitted)	Mar. 2004
1045	Riahi, D. N.	Steady and oscillatory flow in a mushy layer—*Current Topics in Crystal Growth Research*, in press (2004)	Mar. 2004
1046	Riahi, D. N.	Modeling flows in protein crystal growth—*Current Topics in Crystal Growth Research*, in press (2004)	Mar. 2004
1047	Bagchi, P., and S. Balachandar	Response of the wake of an isolated particle to isotropic turbulent cross-flow—*Journal of Fluid Mechanics* (submitted)	Mar. 2004
1048	Brown, E. N., S. R. White, and N. R. Sottos	Fatigue crack propagation in microcapsule toughened epoxy—*Journal of Materials Science* (submitted)	Apr. 2004
1049	Zeng, L., S. Balachandar, and P. Fischer	Wall-induced forces on a rigid sphere at finite Reynolds number—*Journal of Fluid Mechanics* (submitted)	May 2004
1050	Dolbow, J., E. Fried, and H. Ji	A numerical strategy for investigating the kinetic response of stimulus-responsive hydrogels—*Computer Methods in Applied Mechanics and Engineering* **194**, 4447–4480 (2005)	June 2004
1051	Riahi, D. N.	Effect of permeability on steady flow in a dendrite layer—*Journal of Porous Media*, in press (2004)	July 2004
1052	Cermelli, P., E. Fried, and M. E. Gurtin	Transport relations for surface integrals arising in the formulation of balance laws for evolving fluid interfaces—*Journal of Fluid Mechanics* (submitted)	Sept. 2004
1053	Stewart, D. S., and A. R. Kasimov	Theory of detonation with an embedded sonic locus—*SIAM Journal on Applied Mathematics* (submitted)	Oct. 2004
1054	Stewart, D. S., K. C. Tang, S. Yoo, M. Q. Brewster, and I. R. Kuznetsov	Multi-scale modeling of solid rocket motors: Time integration methods from computational aerodynamics applied to stable quasi-steady motor burning—*Proceedings of the 43rd AIAA Aerospace Sciences Meeting and Exhibit* (January 2005), Paper AIAA-2005-0357 (2005)	Oct. 2004
1055	Ji, H., H. Mourad, E. Fried, and J. Dolbow	Kinetics of thermally induced swelling of hydrogels—*International Journal of Solids and Structures* (submitted)	Dec. 2004
1056	Fulton, J. M., S. Hussain, J. H. Lai, M. E. Ly, S. A. McGough, G. M. Miller, R. Oats, L. A. Shipton, P. K. Shreeman, D. S. Widrevitz, and E. A. Zimmermann	Final reports: Mechanics of complex materials, Summer 2004 (K. M. Hill and J. W. Phillips, eds.)	Dec. 2004
1057	Hill, K. M., G. Gioia, and D. R. Amaravadi	Radial segregation patterns in rotating granular mixtures: Waviness selection—*Physical Review Letters* **93**, 224301 (2004)	Dec. 2004
1058	Riahi, D. N.	Nonlinear oscillatory convection in rotating mushy layers—*Journal of Fluid Mechanics*, in press (2005)	Dec. 2004
1059	Okhuysen, B. S., and D. N. Riahi	On buoyant convection in binary solidification—*Journal of Fluid Mechanics* (submitted)	Jan. 2005
1060	Brown, E. N., S. R. White, and N. R. Sottos	Retardation and repair of fatigue cracks in a microcapsule toughened epoxy composite—Part I: Manual infiltration—*Composites Science and Technology* (submitted)	Jan. 2005
1061	Brown, E. N., S. R. White, and N. R. Sottos	Retardation and repair of fatigue cracks in a microcapsule toughened epoxy composite—Part II: *In situ* self-healing—*Composites Science and Technology* (submitted)	Jan. 2005

List of Recent TAM Reports (cont'd)

No.	*Authors*	*Title*	*Date*
1062	Berfield, T. A., R. J. Ong, D. A. Payne, and N. R. Sottos	Residual stress effects on piezoelectric response of sol-gel derived PZT thin films—*Journal of Applied Physics* (submitted)	Apr. 2005
1063	Anderson, D. M., P. Cermelli, E. Fried, M. E. Gurtin, and G. B. McFadden	General dynamical sharp-interface conditions for phase transformations in viscous heat-conducting fluids—*Journal of Fluid Mechanics* (submitted)	Apr. 2005
1064	Fried, E., and M. E. Gurtin	Second-gradient fluids: A theory for incompressible flows at small length scales—*Journal of Fluid Mechanics* (submitted)	Apr. 2005
1065	Gioia, G., and F. A. Bombardelli	Localized turbulent flows on scouring granular beds—*Physical Review Letters*, in press (2005)	May 2005
1066	Fried, E., and S. Sellers	Orientational order and finite strain in nematic elastomers—*Journal of Chemical Physics* **123**, 044901 (2005)	May 2005
1067	Chen, Y.-C., and E. Fried	Uniaxial nematic elastomers: Constitutive framework and a simple application—*Proceedings of the Royal Society of London A*, in press (2005)	June 2005
1068	Fried, E., and S. Sellers	Incompatible strains associated with defects in nematic elastomers—*Journal of Chemical Physics*, in press (2005)	Aug. 2005
1069	Gioia, G., and X. Dai	Surface stress and reversing size effect in the initial yielding of ultrathin films—*Journal of Applied Mechanics*, in press (2005)	Aug. 2005
1070	Gioia, G., and P. Chakraborty	Turbulent friction in rough pipes and the energy spectrum of the phenomenological theory—*arXiv:physics* 0507066 v1 8 Jul 2005	Aug. 2005
1071	Keller, M. W., and N. R. Sottos	Mechanical properties of capsules used in a self-healing polymer—*Experimental Mechanics* (submitted)	Sept. 2005
1072	Chakraborty, P., G. Gioia, and S. Kieffer	Volcán Reventador's unusual umbrella	Sept. 2005
1073	Fried, E., and S. Sellers	Soft elasticity is not necessary for striping in nematic elastomers—*Nature Physics* (submitted)	Sept. 2005
1074	Fried, E., M. E. Gurtin, and Amy Q. Shen	Theory for solvent, momentum, and energy transfer between a surfactant solution and a vapor atmosphere—*Physical Review E* (submitted)	Sept. 2005
1075	Chen, X., and E. Fried	Rayleigh–Taylor problem for a liquid–liquid phase interface—*Journal of Fluid Mechanics* (submitted)	Oct. 2005
1076	Riahi, D. N.	Mathematical modeling of wind forces—In *The Euler Volume* (Abington, UK: Taylor and Francis), in press (2005)	Oct. 2005
1077	Fried, E., and R. E. Todres	Mind the gap: The shape of the free surface of a rubber-like material in the proximity to a rigid contactor—*Journal of Elasticity*, in press (2006)	Oct. 2005
1078	Riahi, D. N.	Nonlinear compositional convection in mushy layers—*Journal of Fluid Mechanics* (submitted)	Dec. 2005
1079	Bhattacharjee, P., and D. N. Riahi	Mathematical modeling of flow control using magnetic fluid and field—In *The Euler Volume* (Abington, UK: Taylor and Francis), in press (2005)	Dec. 2005
1080	Bhattacharjee, P., and D. N. Riahi	A hybrid level set/VOF method for the simulation of thermal magnetic fluids—*International Journal for Numerical Methods in Engineering* (submitted)	Dec. 2005
1081	Bhattacharjee, P., and D. N. Riahi	Numerical study of surface tension driven convection in thermal magnetic fluids—*Journal of Crystal Growth* (submitted)	Dec. 2005
1082	Riahi, D. N.	Inertial and Coriolis effects on oscillatory flow in a horizontal dendrite layer—*Transport in Porous Media* (submitted)	Jan. 2006
1083	Wu, Y., and K. T. Christensen	Population trends of spanwise vortices in wall turbulence—*Journal of Fluid Mechanics* (submitted)	Jan. 2006
1084	Natrajan, V. K., and K. T. Christensen	The role of coherent structures in subgrid-scale energy transfer within the log layer of wall turbulence—*Physics of Fluids* (submitted)	Jan. 2006